crystals

MDPI

Article

Fast One-Step Microwave-Assisted Synthesis of Iron-Doped ZnS for Photocatalytic Applications

Sonia J. Bailón-Ruiz [1,*], Yarilyn Cedeño-Mattei [1], Angelie M. Núñez-Colón [2] and Kerianys Torres-Torres [2]

[1] Department of Chemistry and Physics, University of Puerto Rico in Ponce, Ponce, PR 00716, USA; yarilyn.cedeno@upr.edu
[2] Department of Biology, University of Puerto Rico in Ponce, Ponce, PR 00716, USA; angelie.nunez@upr.edu (A.M.N.-C.); kerianys.torres@upr.edu (K.T.-T.)
* Correspondence: sonia.bailon@upr.edu

Abstract: Semiconductor Zn-based nanomaterials have emerged as promising agents for the photocatalytic degradation of organic pollutants in wastewater treatment. However, achieving efficient synthesis protocols capable of rapidly producing small structures directly in aqueous environments remains challenging. Microwave-assisted synthesis presents a viable solution by enabling one-step particle generation swiftly and directly in water through increased pressure, thereby easily elevating the boiling point. This study investigates the microwave-assisted one-step synthesis of pure and iron-doped ZnS nanoparticles and assesses their efficacy in photodegrading Quinoline Yellow (QY) in aqueous suspensions. The results demonstrate a significant degradation of QY in the presence of 1% iron-doped ZnS nanoparticles, achieving approximately 66.3% degradation with 500 ppm of doped nanoparticles after 270 min. These findings highlight the considerable potential of 1% iron-doped ZnS nanoparticles as effective nanocatalysts.

Keywords: Fe-doped ZnS; microwave-assisted synthesis; photodegradation; Quinoline Yellow dye

Citation: Bailón-Ruiz, S.J.; Cedeño-Mattei, Y.; Núñez-Colón, A.M.; Torres-Torres, K. Fast One-Step Microwave-Assisted Synthesis of Iron-Doped ZnS for Photocatalytic Applications. *Crystals* **2024**, *14*, 699. https://doi.org/10.3390/cryst14080699

Academic Editor: Benilde F. O. Costa

Received: 15 July 2024
Revised: 27 July 2024
Accepted: 29 July 2024
Published: 1 August 2024

1. Introduction

Zinc-based nanoparticles like zinc oxide (ZnO), zinc sulfide (ZnS), and zinc selenide (ZnSe) have garnered significant attention due to their unique optical, electrical, and chemical properties, making them suitable for various industrial and biomedical applications. ZnO nanoparticles, with a wide bandgap and high exciton binding energy, are useful in optoelectronics such as UV lasers and light-emitting diodes (LEDs) [1,2] and exhibit significant antimicrobial properties for medical and sanitary applications [3–8], as well as drug delivery systems [6–8]. ZnS nanoparticles are recognized for their strong photoluminescence, making them valuable in bioimaging and sensor applications [9–11], and are also beneficial for optical coatings [12,13] due to their high refractive index and low visible light absorption. ZnSe nanoparticles, with a direct bandgap suitable for blue light-emitting devices [14,15], offer high luminescence efficiency for photonic applications and are advantageous in biomedical imaging for deep tissue imaging [16,17].

Zinc-based nanoparticles hold significant potential for environmental applications due to their remarkable photocatalytic properties [18–24]. These properties arise from their ability to generate reactive oxygen species (ROS) through the electron-hole pair mechanism when exposed to electromagnetic radiation. Upon absorption of UV or visible light, the nanoparticles excite electrons from the valence band to the conduction band, creating electron-hole pairs. These pairs then migrate to the nanoparticle surface where they participate in redox reactions, producing superoxide radicals ($O_2\bullet^-$) and hydroxyl radicals (•OH). These radicals are highly reactive and can degrade a wide range of organic pollutants, making zinc-based nanoparticles effective photocatalysts.

Doping zinc-based nanoparticles involves introducing small amounts of foreign elements to modify and enhance their properties. Metal doping with elements like silver (Ag),

gold (Au), or copper (Cu) can further enhance the photocatalytic activity by increasing charge separation efficiency and extending the light absorption range [25,26]. Ag-doped ZnO nanoparticles demonstrate improved photocatalytic performance due to the plasmonic effect of Ag, which enhances light absorption and reduces the recombination rate of electron-hole pairs. Metal dopants can create surface plasmon resonance (SPR) effects, increasing the local electric field around the nanoparticles, enhancing light absorption, and facilitating the transfer of photogenerated electrons and holes, thereby improving photocatalytic efficiency [27,28].

Zinc-based nanoparticles doped with magnetic ions can act as dilute magnetic semiconductors (DMS), combining semiconducting and magnetic properties. Doping with transition metals like cobalt (Co) and iron (Fe) enhances the magnetic properties [29–33] due to the unpaired d-electrons of these metals. Co-doped ZnO nanoparticles exhibit enhanced ferromagnetic properties because of interactions between Co ions and the ZnO lattice [34–36]. This effect is due to exchange interactions between the dopant's d-electrons and the host material's electrons, enabling long-range ferromagnetic ordering at room temperature. Fe-doped ZnS nanoparticles demonstrate room-temperature ferromagnetism, making them suitable for spintronic device applications [37].

The synthesis of zinc-based nanoparticles often involves organic solvents, presenting several disadvantages. These non-environmental methods, like sol-gel and solvothermal processes, require prolonged reaction times and complex multi-step procedures, leading to extensive purification steps that add to the complexity and cost while generating additional waste and environmental pollution [38–41]. Organic solvents often result in larger particle sizes, reducing the surface area and catalytic effectiveness of the nanoparticles. Additionally, these methods are often non-reproducible due to sensitivity to minor variations in reaction conditions, hindering scalability and commercial viability. The nanoparticles produced are usually not water-stable, leading to aggregation in aqueous solutions, which decreases their effective surface area and catalytic efficiency, limiting their use in water purification and environmental remediation.

The need for clean technologies like microwave-assisted methods to synthesize zinc-based nanomaterials has become apparent due to the environmental and functional limitations of traditional methods. Microwave-assisted synthesis is an efficient and rapid technique that uses microwave radiation for uniform heating, significantly reducing reaction times and enhancing reaction kinetics. This method produces nanoparticles with controlled size and morphology, high purity, and improved crystallinity while requiring fewer reagents and generating less waste, aligning with green chemistry principles. It can be performed in aqueous solutions, eliminating the need for toxic organic solvents and enhancing the water stability of the nanoparticles for environmental applications. Zinc-based nanoparticles synthesized this way, such as zinc oxide and zinc sulfide, show improved photocatalytic, antimicrobial, and luminescent properties [42–45]. Additionally, this method has been used to create other nanomaterials like titanium dioxide (TiO_2) [46], gold (Au) [47,48], silver (Ag) [49], reduced graphene oxide (rGO) [50,51], and iron oxide (Fe_3O_4) nanoparticles [52], among others.

To the best of our knowledge, Fe-doped ZnS quantum dots have not been synthesized using microwave technology, highlighting a significant gap in the current research. This study intended to generate iron-doped ZnS nanostructures with enhanced photocatalytic properties through microwave-assisted synthesis. The presence of iron is expected to improve the photocatalytic properties of ZnS by facilitating the separation of electron-hole pairs and increasing the absorption of visible light. This enhancement occurs because iron ions can introduce additional energy levels within the bandgap of ZnS, thereby reducing the recombination rate of photogenerated charge carriers and allowing more efficient utilization of the solar spectrum. Consequently, the overall photocatalytic efficiency of iron-doped ZnS is significantly improved compared to pure ZnS, making it a promising candidate for environmental remediation applications.

Quinoline Yellow (QY), a synthetic yellow dye widely used in various industries, poses significant environmental concerns due to its presence in water bodies. It is commonly used as a colorant in food products, beverages, cosmetics, and pharmaceuticals, known by its European food additive number, E104. Despite its widespread use, QY has raised health and safety concerns, including potential hyperactivity in children and allergic reactions, leading to regulatory restrictions or bans in some regions, such as Japan [53]. The dye's environmental impact is also troubling, particularly its toxicity and persistence in water bodies. These issues highlight the need for careful regulation and potential alternatives to mitigate its adverse effects on human health and the environment.

In this study, Quinoline Yellow dye has been employed as a model pollutant to study the photocatalytic properties of pure and Fe-doped ZnS nanoparticles. Researchers have employed Quinoline Yellow to assess the enhanced photocatalytic activity of Fe-doped ZnS compared to pure ZnS, demonstrating that the presence of iron dopants improves the degradation rate of the dye. The improved performance is attributed to the enhanced separation of electron-hole pairs and increased visible light absorption facilitated by the Fe-doping, which collectively boosts the photocatalytic efficiency of ZnS nanoparticles.

Pure and Fe-doped ZnS nanoparticles were synthesized using a fast, single-step microwave-assisted synthesis method. The synthesized nanoparticles were characterized using various techniques, including high-resolution transmission electron microscopy (HRTEM), X-ray diffraction (XRD), vibrating sample magnetometry (VSM), UV-visible spectroscopy (UV-Vis), and photoluminescence (PL). Additionally, the photocatalytic properties of these nanoparticles were evaluated using Quinoline Yellow dye as a model pollutant. The results demonstrated that Fe-doping enhanced the photocatalytic efficiency of ZnS nanoparticles, facilitating improved degradation of the dye compared to pure ZnS.

2. Materials and Methods

2.1. Materials

Zinc sulphate heptahydrate ($ZnSO_4.7H_2O$, ReagentPlus® $\geq$ 99.0%, Sigma Aldrich, St. Louis, MO, USA), sodium sulfide (Na_2S 3% *w*/*w*, Ricca Chemical, Arlington, TX, USA), and iron sulfate heptahydrate ($FeSO_4.7H_2O$, ReagentPlus® $\geq$ 99.0%, Sigma Aldrich, St. Louis, MO, USA) were employed in the nanoparticles' synthesis. Quinoline Yellow ($C_{18}H_9NNa_2O_8S_2$, Sigma Aldrich, St. Louis, MO, USA) was used for the photocatalysis experiments. Isopropanol ($(CH_3)_2CHOH$, $\geq$99.7% for HPLC, BeanTown Chemical, Hudson, NH, USA) was acquired for purification of the nanoparticles. Ultrapure water was used in all the experiments. The reagents were used without further purification.

2.2. Generation of Pure and Iron-Doped ZnS Nanoparticles

Pure ZnS nanoparticles were synthesized using a microwave digestion system, MARS 6, from CEM Corporation. The synthesis involved introducing a zinc sulfate heptahydrate solution (0.4 M) and a sulfur source (3% *w*/*w* Na_2S) into the reaction mixture, which consisted of 5.0 mL of zinc solution and 2.5 mL of Na_2S solution. This mixture was then placed in a Teflon vessel and heated at 140 °C for 15 min in the microwave digestion system with a frequency of 2.45 GHz. These specific temperature and time conditions were selected based on preliminary studies that showed higher temperatures and longer reaction times led to reduced nanoparticle stability in water and increased agglomeration [54].

Iron-doped ZnS nanoparticles with enhanced photoactive properties were produced using the same precursors as those for pure ZnS synthesis but with the addition of a 0.15 M solution of iron sulfate heptahydrate to the reaction mixture. The mixture was then placed in a Teflon vessel and heated at 140 °C for 15 min in the microwave digestion system. The doping levels of iron (II) were set at 1%, 3%, and 5% *w*/*w*. This systematic method enabled us to examine the effects of different iron doping concentrations on the properties of ZnS nanoparticles.

The as-synthesized colloidal pure and doped nanoparticles were purified using isopropanol, centrifuged at 5000 rpm for 15 min, and then resuspended in deionized water for further characterization.

2.3. Characterization of Pure and Iron-Doped ZnS Nanoparticles

The morphology was analyzed by high-resolution transmission electron microscopy (HRTEM) using a JEM-ARM200cF (JEOL, Akishima, Tokyo, Japan) microscope at 200 kV. The instrument is equipped with an energy-dispersive X-ray spectrometer (EDS) (Oxford Aztec, High Wycombe, UK). The pure and iron-doped ZnS crystalline structure was determined by X-ray diffraction (XRD) in a Siemens Powder Diffractometer D5000 using Cu-K radiation (Siemens, Munich, Germany). The UV-visible absorption spectra of pure and iron-doped ZnS nanoparticles were monitored in the spectral range of 200–900 nm using a UV-2700i spectrophotometer (Shimadzu, Columbia, MD, USA). Photoluminescence properties were studied using an RF-6000 spectrofluorometer (Shimadzu, Columbia, MD, USA). Additionally, the magnetic properties of the synthesized nanomaterials were studied using a 7400 series vibrating sample magnetometer (VSM) (LakeShore, Westerville, OH, USA).

2.4. Photocatalytic Experiments of Quinoline Yellow

The protocol for the photocatalytic degradation of Quinoline Yellow (QY) using pure and 1% Fe-doped ZnS nanoparticles followed previously published methods [55–57]. A 500 μM stock solution was prepared, from which nine standard solutions with concentrations ranging from 1 μM to 40 μM were made to monitor their absorbance and determine the wavelength of maximum absorbance. The concentrations of pure and Fe-doped ZnS nanoparticles were set at 250 ppm and 500 ppm. Experimental solutions were prepared with a QY concentration of 20 μM in an aqueous medium, each concentration being prepared in triplicate, resulting in six solutions in total. Additionally, control solutions containing only 20 μM of the dye in deionized water were prepared. These control solutions, labeled as QY-light and QY-dark, were used to compare the degradation progress with the experimental solutions containing both the nanoparticles and the dye.

The experimental and control solutions underwent photocatalytic degradation using an 8 watt UV lamp emitting at 302 nm, delivering an irradiance of 10 mW/cm^2 at room temperature, with agitation at 24 rpm using a rotamix. The QY-dark control solution was kept in a darkened environment under identical conditions. Samples were collected every 30 min and analyzed using a UV-Vis Spectrophotometer 2700i (Shimadzu, Columbia, MD, USA) to measure absorbance and monitor the degradation progress of Quinoline Yellow. The samples were assessed at the specific absorption peak of 413 nm for QY, determined from the absorbance spectra of previously prepared standard solutions. The reduction in dye concentration over time was determined using a calibration curve. The absorbance calibration curve for Quinoline Yellow was plotted for concentrations ranging from 1 μM to 40 μM, and the line equation and correlation coefficient were determined from this calibration curve.

3. Results and Discussion

3.1. Morphological, Compositional, and Optical Characterization

Microwave heating offers a significant advantage in nanoparticle synthesis due to its ability to rapidly transfer energy through radiation rather than conventional heat transfer or convection. This facilitates immediate energy penetration into materials transparent to microwave radiation, ensuring instantaneous heating. The use of microwave treatment not only reduces reaction times, enhances yields, and improves selectivities but also minimizes energy and reagent consumption. Additionally, employing microwave-energy pulses provides an additional reduction in overall energy usage. Dielectric polarization plays a crucial role in this process, particularly in the presence of polar compounds such as water. This mechanism efficiently absorbs microwave energy, facilitating rapid and uniform heating of the reaction medium essential for the synthesis of pure and doped ZnS nanoparticles. It

enables the breakdown of precursor molecules (e.g., zinc sulfate, sodium sulfide, and iron sulfate), promoting nucleation and growth processes, and influencing the size, morphology, and crystalline structure of both pure and doped nanoparticles. Together, these aspects underscore the effectiveness of microwave-assisted synthesis in achieving efficient and controlled nanoparticle fabrication [58].

High-resolution transmission electron microscopy (HRTEM) was employed to examine the shape and size of the synthesized nanoparticles. Figures 1–4 depict pure and Fe-doped ZnS nanoparticles, revealing their nanometric size (less than 5 nm) and predominantly spherical morphology. These images clearly illustrate the crystalline structure of the nanoparticles.

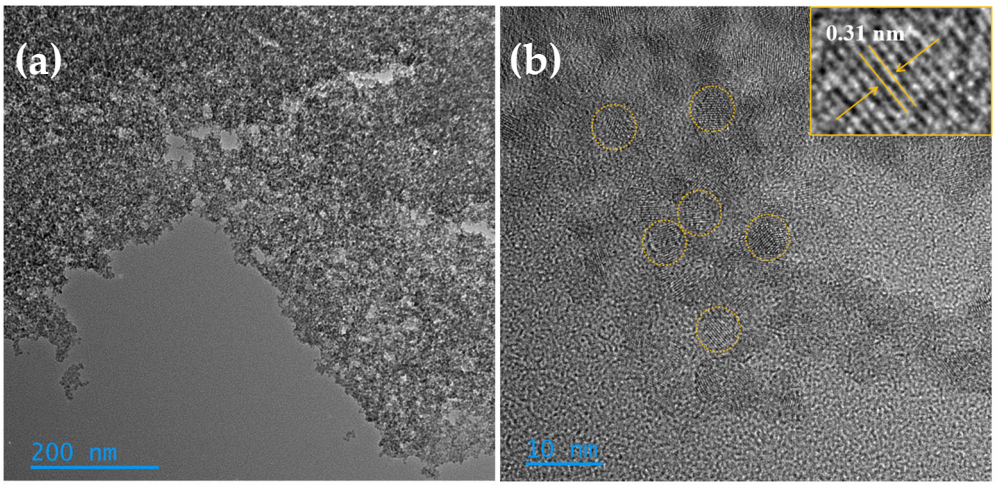

Figure 1. Low magnification TEM image (**a**) and HRTEM image (**b**) of pure ZnS nanoparticles.

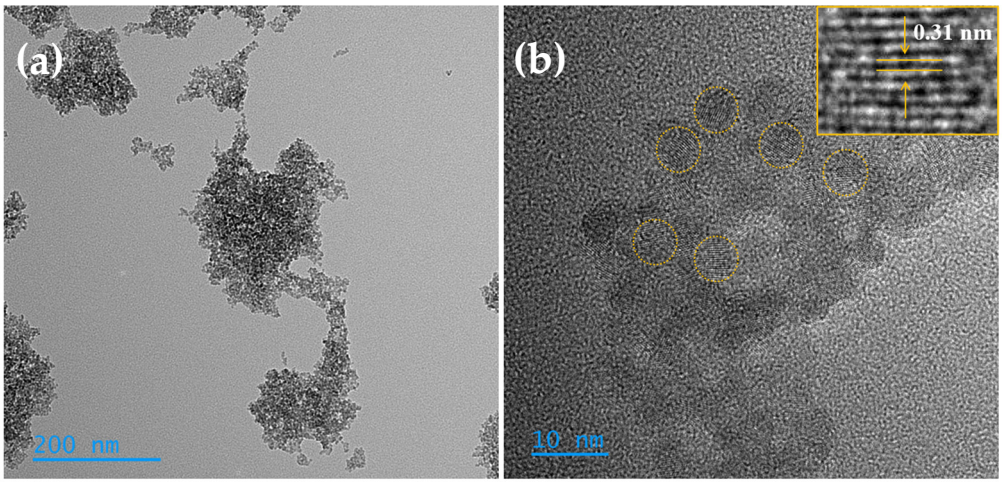

Figure 2. Low magnification TEM image (**a**) and HRTEM image (**b**) of 1% Fe–doped ZnS nanoparticles.

The morphology of pure ZnS nanoparticles is depicted in Figure 1a,b, with an average size of approximately 4 nm. Energy-dispersive X-ray spectroscopy (EDS) studies confirmed the elemental composition of the nanoparticles, showing 46.91% zinc and 53.09% sulfur. HRTEM further validated the crystallinity of the ZnS nanoparticles (Figure 1b). The lattice spacing for the nanomaterials, as shown in the inset of Figure 1b, measured approximately 0.31 ± 0.01 nm, corresponding to the (111) plane of a cubic structure [59–61]. This average was determined from ten measurements using ImageJ software (version 1.54j).

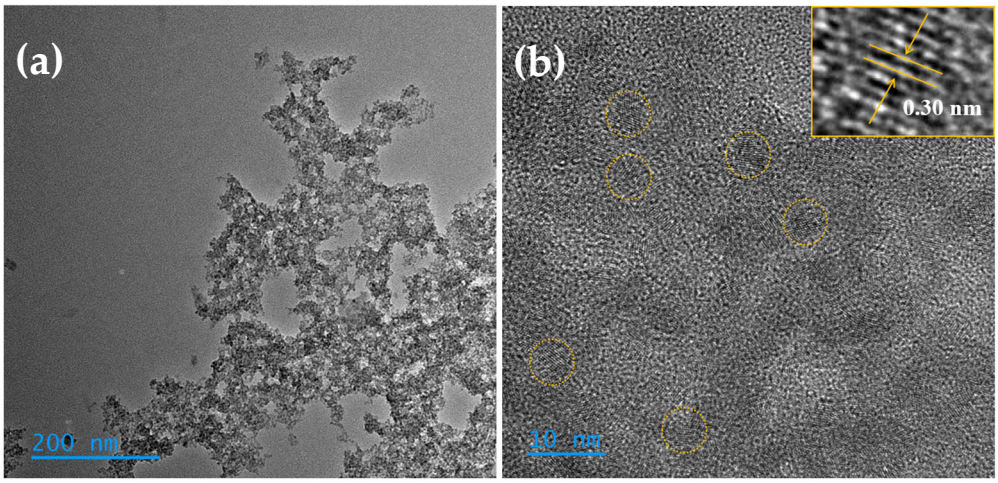

Figure 3. Low magnification TEM image (**a**) and HRTEM image (**b**) of 3% Fe-doped ZnS nanoparticles.

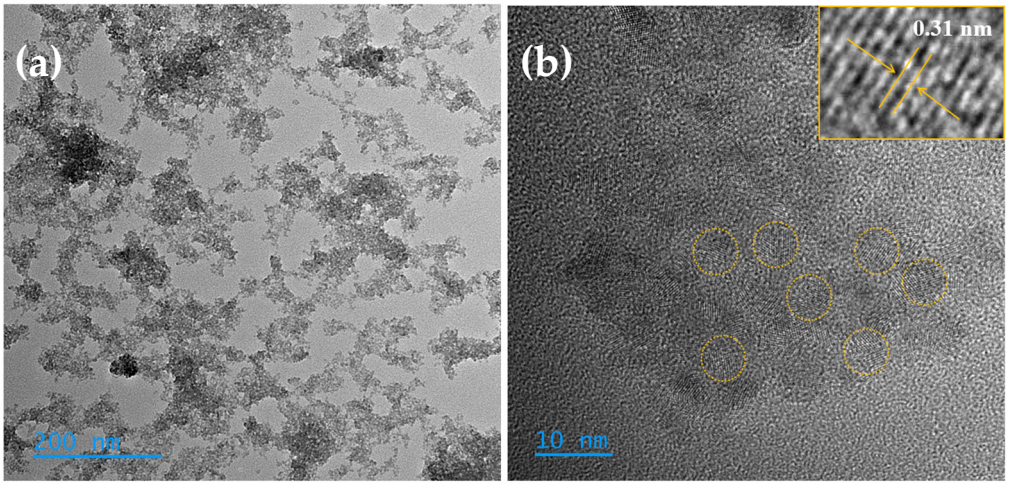

Figure 4. Low magnification TEM image (**a**) and HRTEM image (**b**) of 5% Fe–doped ZnS nanoparticles.

Figures 2–4 present TEM images of Fe-doped ZnS nanoparticles at both low and high resolutions, demonstrating that the nanoparticle size undergoes minimal change upon doping, remaining consistently below 5 nm. EDS analyses indicated a trace amount of Fe in the samples, ranging from 0.5 to 1.6 atomic percent. The doped samples also exhibited zinc and sulfur as the primary components. The lattice spacing for the doped samples with 1%, 3%, and 5% Fe doping was measured at 0.31 ± 0.01 nm, 0.30 ± 0.02 nm, and 0.30 ± 0.01 nm, respectively (inset of Figures 2b, 3b and 4b). These values correspond to the (111) plane, confirming that the iron-doped nanoparticles retain the same face-centered cubic (FCC) crystalline structure as pure ZnS.

Figure 5 displays the X-ray diffraction (XRD) patterns of pure ZnS and Fe-doped ZnS nanoparticles. The diffraction patterns feature three prominent peaks around 29°, 48°, and 57° representing the (111), (220), and (311) lattice planes, respectively. These peaks align with the face-centered cubic (FCC) structure of ZnS. The average crystallite size of pure ZnS and Fe-doped ZnS was determined using Scherrer's equation, based on the diffraction peak (111). For pure ZnS, the average crystallite size was estimated to be 2.7 nm. In contrast, all Fe-dopant concentrations exhibited a larger average crystallite size of 3.4 nm. The average crystallite sizes calculated using XRD data are in good agreement with the particle sizes measured by HRTEM (smaller than 5 nm). The increase in average crystallite size from 2.7 nm in pure ZnS to 3.4 nm in Fe-doped ZnS nanoparticles can be attributed to several factors. One primary reason is the difference in ionic radii between Zn^{2+} (0.074 nm) and

Fe^{2+} (0.077 nm). When Fe ions are incorporated into the ZnS lattice, they can cause lattice distortion due to their different sizes, which can influence the crystallization process and result in the formation of larger crystallites. Furthermore, the presence of Fe can alter the nucleation and growth kinetics of the ZnS nanoparticles, promoting the growth of larger crystallites. This effect is often observed in doped semiconductor materials, where the dopant can modify the energy barriers for nucleation and growth, leading to changes in crystallite size.

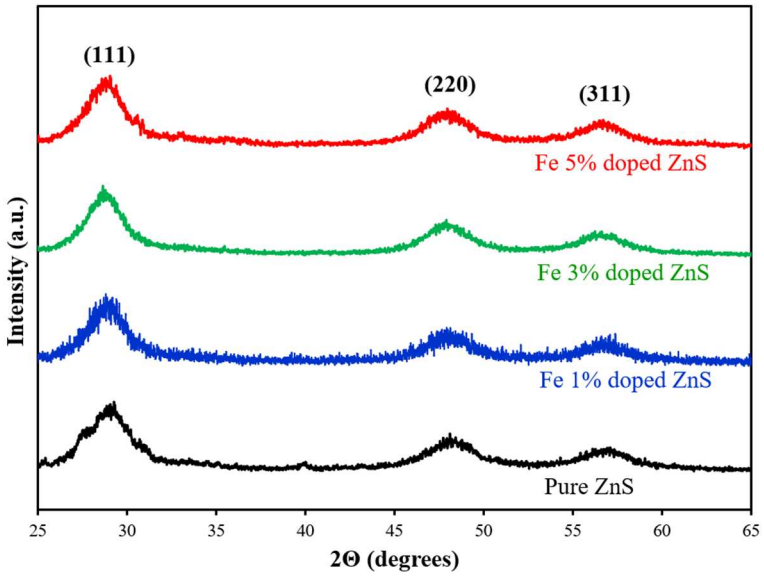

Figure 5. XRD patterns of pure ZnS and 1% Fe, 3% Fe, and 5% Fe–doped ZnS nanoparticles.

The magnetic properties of dilute magnetic semiconductors (DMS) near room temperature (RT) are crucial for numerous practical applications. To better understand the magnetic behavior of Fe-doped ZnS nanoparticles, hysteresis loops (magnetization versus applied magnetic field curves) were measured at room temperature, as shown in Figure 6. Pure ZnS exhibits diamagnetic behavior, whereas Fe-doped ZnS nanoparticles display room-temperature ferromagnetism (RTFM) with magnetization increasing as Fe content rises. The magnetizations for the 1%, 3%, and 5% Fe-doped ZnS nanoparticles are 0.016, 0.072, and 0.16 emu/g, respectively. None of the samples showed signs of saturation.

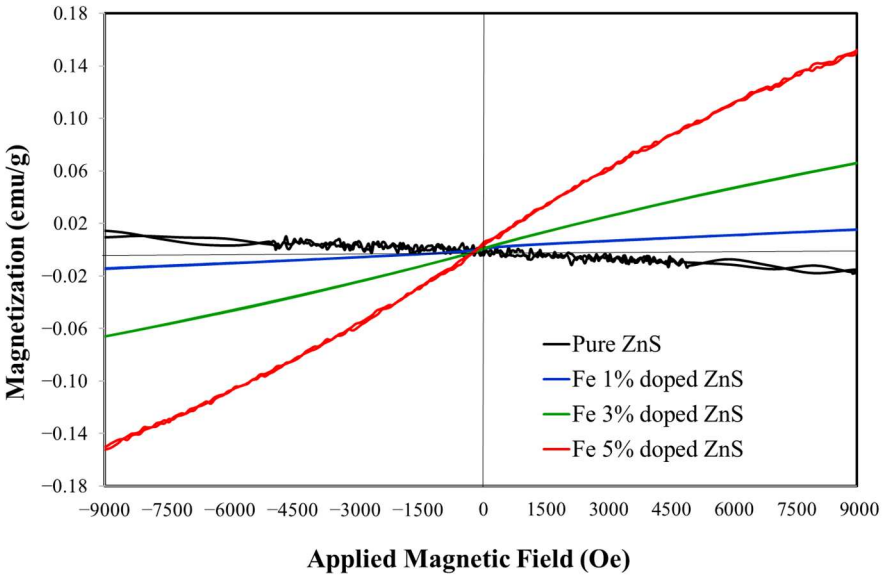

Figure 6. Hysteresis loops of pure ZnS and 1% Fe, 3% Fe, and 5% Fe–doped ZnS nanoparticles.

Room temperature ferromagnetism in Fe-doped ZnS arises from the introduction of iron atoms into the ZnS lattice, which creates magnetic moments due to unpaired electrons in the Fe atoms' d-orbitals. These magnetic moments interact through exchange interactions, which can be direct or mediated by the sulfur atoms in the ZnS structure, known as the super-exchange mechanism. The doping process also introduces defects and vacancies in the lattice, further enhancing the interactions between Fe atoms. These interactions are strong enough to maintain ferromagnetic order at room temperature. The resulting room temperature ferromagnetism in Fe-doped ZnS opens possibilities for applications in spintronics and magnetic sensors, leveraging both the electrical and magnetic properties of the material.

Figure 7 displays the UV-absorption spectra of pure and iron-doped ZnS nanoparticles in colloidal solution at concentrations of 0.02 g for all samples. A characteristic peak in the UV region (~316 nm) is observed for all samples, attributed to intrinsic absorption where electrons suffer transitions from the valence band to the conduction band. The blue shift of the absorption bands in pure and iron-doped ZnS compared to ZnS bulk (336 nm) can be attributed to the quantum size effect, observed when nanostructures approach or are smaller than the Bohr exciton radius [62–64].

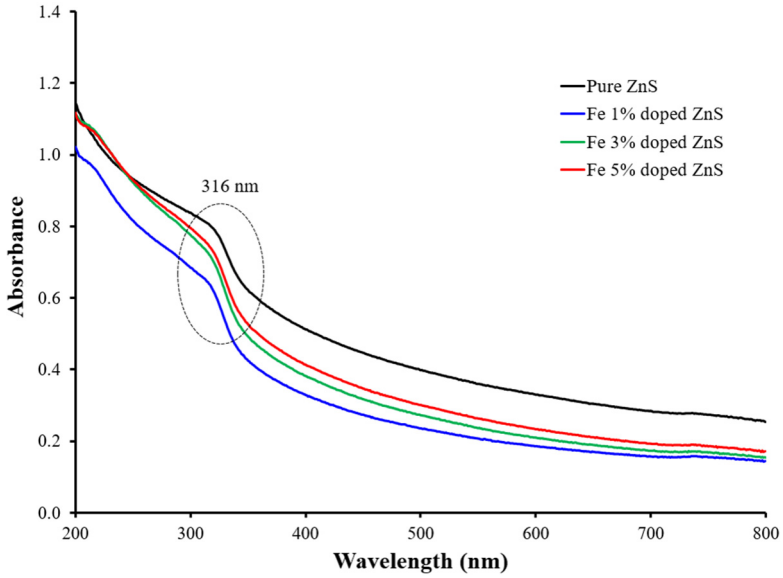

Figure 7. Absorbance spectra of pure ZnS and 1% Fe, 3% Fe, and 5% Fe–doped ZnS nanoparticles.

The band gap energies were estimated using the Tauc equation as 3.35 eV, 3.52 eV, 3.50 eV, and 3.48 eV for pure ZnS, and ZnS doped with 1%, 3%, and 5% Fe, respectively (Figure 8). A redshift in the band gap upon Fe incorporation into ZnS is noted, primarily due to sp-d exchange interactions between the band electrons and the localized d electrons of Fe^{2+} ions substituting Zn^{2+} ions [65,66].

Figure 9 displays the photoluminescence spectra of pure and iron-doped ZnS nanoparticles, recorded at an excitation wavelength of 302 nm. A prominent band gap emission peak around 353 nm is observed exclusively for pure ZnS, attributed to exciton recombination. In contrast, iron-doped ZnS nanoparticles show a notably absent main peak, indicating energy level transitions of Fe ions that quench UV emission. Both pure (at 450 nm) and doped (at 468 nm) nanoparticles exhibit a secondary trap peak in the visible range, attributed to structural defects like sulfur vacancies and zinc interstitials that facilitate a radiative recombination of electrons and photogenerated holes in the crystals. Iron doping introduces additional cations and potentially more anion vacancies (S^{-2}), which can alter the energy level structure of ZnS. Moreover, Fe^{2+} ions replace some Zn^{2+} ions in the crystal lattice, evidenced by the low concentrations of iron ions (less than 1.6%) in the nanoparticles. This substitution is facilitated by the similar ionic radii of Zn^{2+} (0.074 nm) and Fe^{2+} (0.077 nm).

The trap peak initially shifts towards shorter wavelengths in doped ZnS compared to pure ZnS, and its intensity diminishes with increasing Fe concentration (from 1% to 5% Fe). This quenching effect occurs because photo-generated electrons preferentially occupy the trap centers induced by Fe^{2+} ions [67,68].

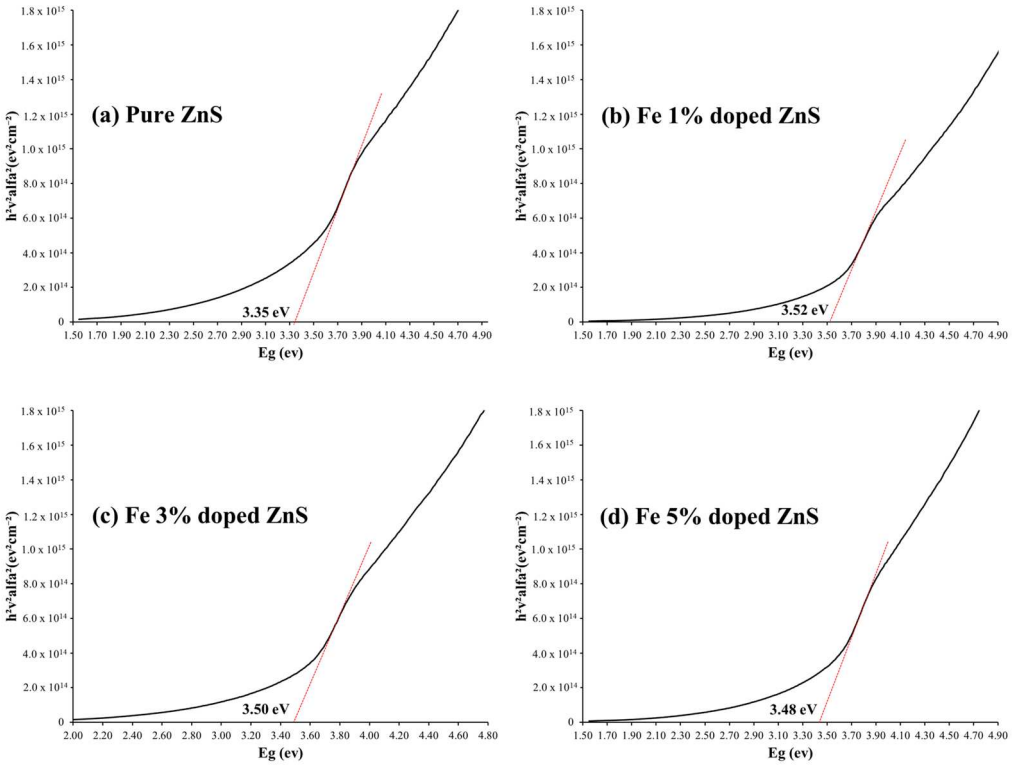

Figure 8. Band gap energies of pure ZnS (**a**) and 1% Fe (**b**), 3% Fe (**c**), and 5% (**d**) Fe–doped ZnS nanoparticles.

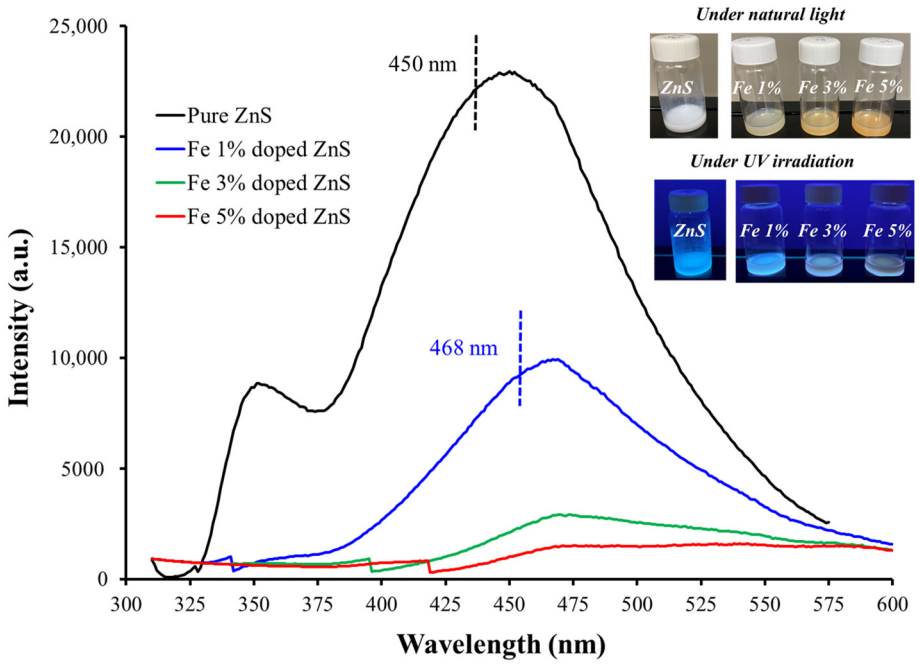

Figure 9. Photoluminescence spectra of pure ZnS and 1% Fe, 3% Fe, and 5% Fe–doped ZnS nanoparticles.

In Figure 9, insets show images of colloidal suspensions of pure and iron-doped ZnS nanoparticles under natural light and UV irradiation. An observable color change from white to orange-brown occurs with increasing dopant concentration (1% to 5% Fe) in the crystals. Additionally, doped nanoparticles demonstrate enhanced stability in water compared to pure ZnS, particularly at lower dopant concentrations (1% Fe). This stability in aqueous media is crucial for subsequent photodegradation studies. Previous studies have noted that low concentrations of iron reduce the dissolution of Zn-based nanostructures, thereby increasing their stability in aqueous environments [69].

3.2. Photodegradation of Quinoline Yellow

Figures 10 and 11 illustrate the degradation of Quinoline Yellow in the presence of pure and 1% iron-doped ZnS nanoparticles at two concentrations (250 ppm and 500 ppm), respectively. As described earlier (in the Section 2), QY degradation was monitored at 413 nm based on the absorption peak of the standard solutions (Figure 12). Throughout the experiment, the relative dye concentration (C_f/C_i) was continuously monitored and recorded. C_f corresponds to the final dye concentration, and C_i corresponds to the initial dye concentration. The ratio C_f:C_i is instrumental in quantifying photodegradation, as it directly reflects the reduction in dye concentration, thereby indicating the efficiency of the photodegradation process.

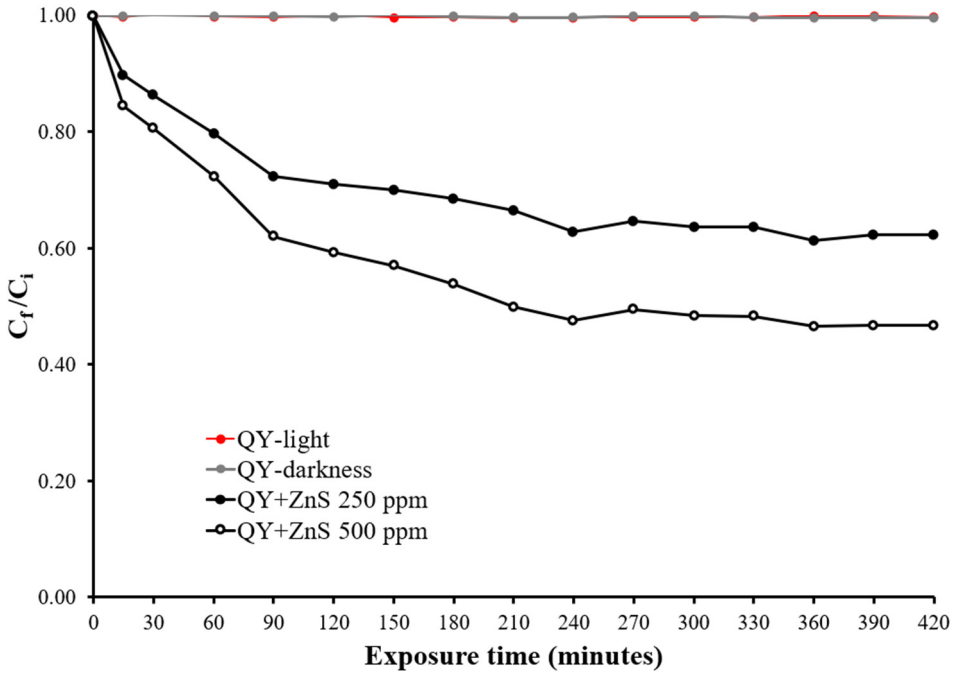

Figure 10. Photodegradation of Quinoline Yellow in the presence of pure ZnS nanoparticles.

The actual dye concentration over time was determined using the calibration curve plotted (Figure 13). The results indicate that the photodegradation process is closely linked to the concentration of the nanocatalyst, the duration of UV irradiation, and the presence of the dopant. Control groups exposed to UV light and those kept in darkness showed minimal degradation, highlighting the persistent nature of QY in aqueous environments due to its stable aromatic structure. Quinoline Yellow is known for its hazardous and recalcitrant nature, characterized by high photolytic stability and low biodegradability [70]. Using 250 ppm of Fe-doped ZnS nanoparticles, approximately 50.9% of QY was degraded, which increased to 66.3% when using 500 ppm during the initial 270 min (Figure 10). In contrast, with 250 ppm and 500 ppm of pure ZnS nanoparticles, a 37.8% and 53.3% degradation of quinoline yellow was achieved within the first 420 min, respectively, with no further degradation observed thereafter (Figure 11). These findings suggest that low concentrations

of iron ions in ZnS crystals enhance the photocatalytic efficacy of these nanoparticles. This enhancement can be attributed to the doped nanoparticles' increased ability to generate reactive oxygen species or to directly interact with Quinoline Yellow molecules through electron-hole pairs, facilitating their degradation. A schematic of the dye degradation using doped-ZnS nanoparticles is shown in Figure 14. Under electromagnetic radiation (e.g., 302 nm), electrons from the valence band (VB) of Fe-doped ZnS nanoparticles are excited to the conduction band (CB). Fe^{2+} ions within the ZnS crystals act as electron traps, capturing CB electrons and promoting interfacial charge-transfer kinetics that inhibit electron-hole recombination. Consequently, VB holes and CB electrons react with water and oxygen molecules to produce hydroxyl and superoxide anion radicals, which facilitate Quinoline Yellow degradation in aqueous environments. [71,72]. Figure 15 shows the pattern of photodegradation of Quinoline Yellow ($C_{18}H_{11}NO_5S$) molecules, ($[M - H]^+$, 353.0358 m/z) under the treatment of light-activated Fe-doped ZnS 500 ppm. These studies were made by using a QTOF-LC-MS, an InfinityLab Poroshell 120 EC−C18 column (Agilent Technologies, Santa Clara, CA, USA), and a mobile phase of 60/40 methanol water with 0.1% formic acid. Five degradation products of QY, labeled P1 to P5, were identified. Among them, P1 has a molecular formula of $C_9H_8NO_3SNa^+$ ($[M - Na]^+$, 233.0123 m/z) and was likely quinoline sulfonic acid, which appeared to form through C–C bond cleavage. The identification of P1 enabled us to locate the sulfonic group on the quinoline ring in QY. The loss of the sulfonic acid group from P1 generated P2 (C_9H_7N) with a mass/charge of 129.0578. P3, with a molecular formula of $C_6H_5O_3S^-$ (156.9965 m/z), may indicate the presence of the benzenesulfonate anion, which was generated from the degradation of P1. Furthermore, the loss of the sulfonic group from Quinoline Yellow results in the formation of the intermediate P4 $[M - H]^+$, with a molecular formula of $C_{18}H_{11}NO_2$ (273.0790 m/z). It is suggested that P4 undergoes cleavage of the five-carbon ring and subsequent carboxylation, leading to the formation of P5. This last product $[M - Na]^+$, shows a molecular formula of $C_8H_5NaO_3$ (172.0136 m/z) and confirms the oxidative effect of the ROS on the degradation route. P5 evidences the capacity of Fe-doped ZnS to break off P4 and the opening of the five-carbon ring, which suggests the mineralization of Quinoline Yellow. In summary, the results demonstrate that iron-doping significantly enhances the photocatalytic activity compared to pure ZnS nanoparticles. The introduction of iron ions into the ZnS lattice creates new energy levels that improve charge separation, reduce electron-hole recombination, and increase reactive oxygen species generation. These findings underscore the potential of iron-doped nanoparticles as effective nanocatalysts for water purification applications.

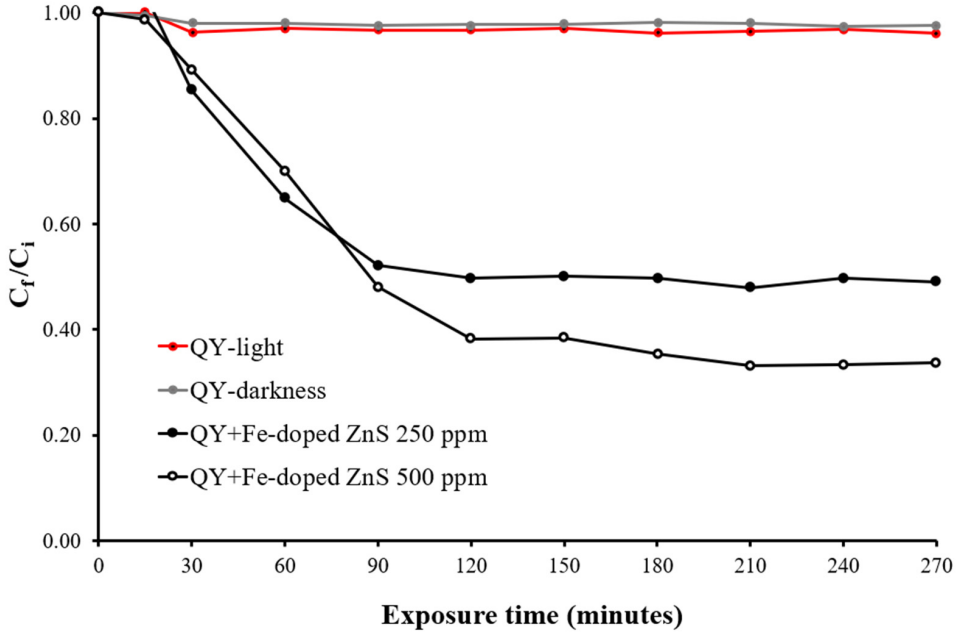

Figure 11. Photodegradation of Quinoline Yellow in the presence of 1% Fe–doped ZnS nanoparticles.

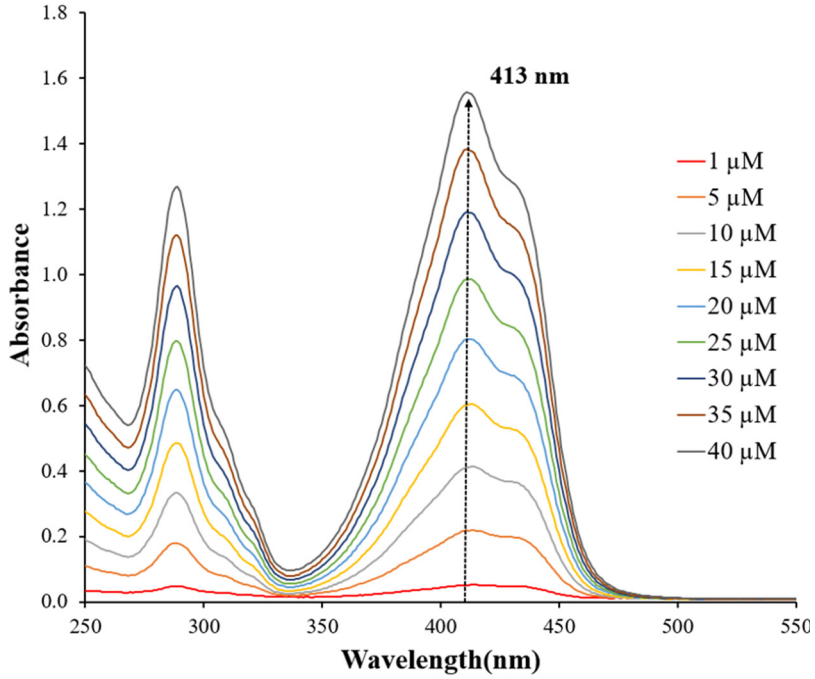

Figure 12. Absorbance spectra of Quinoline Yellow standard solutions.

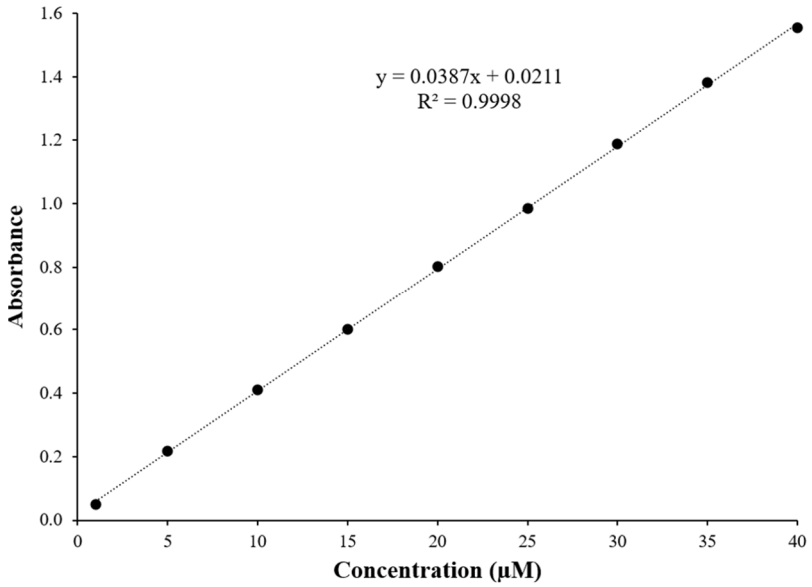

Figure 13. Calibration curve of Quinoline Yellow.

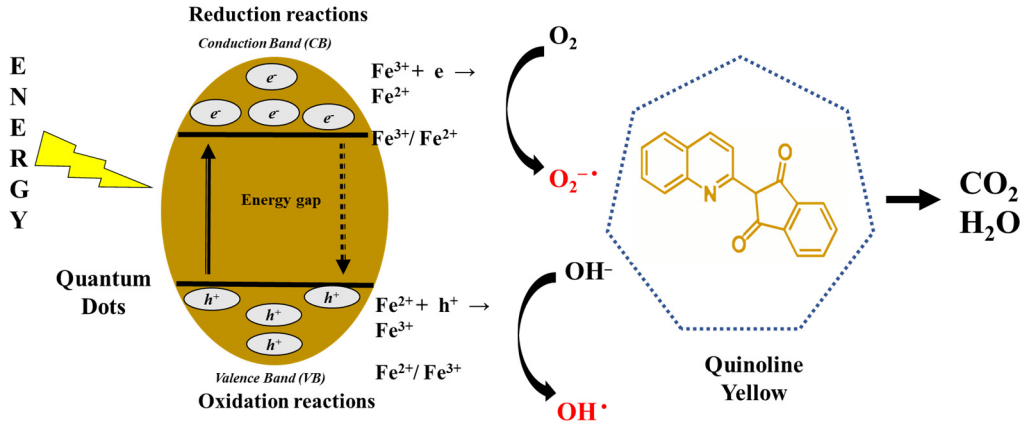

Figure 14. Schematic of Quinoline Yellow degradation in the presence of Fe–doped ZnS.

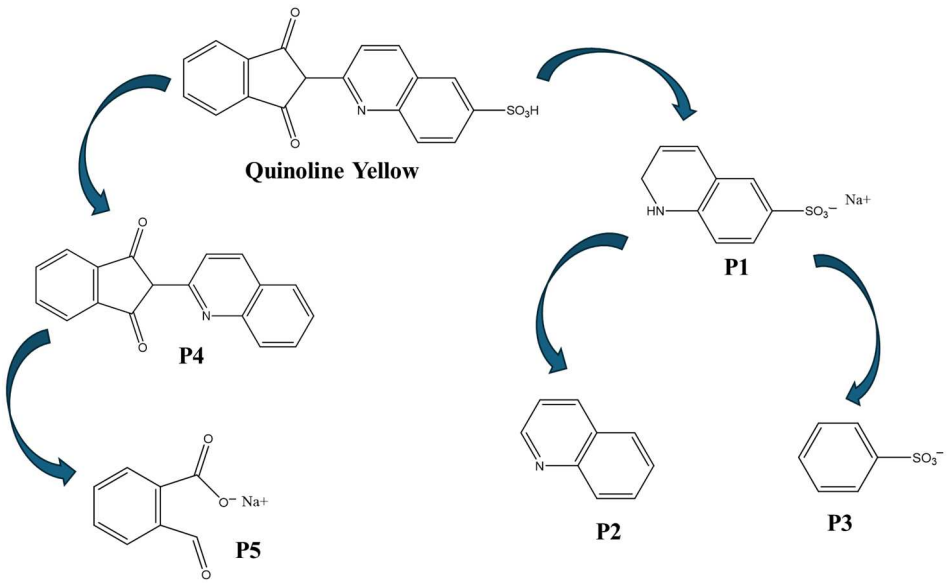

Figure 15. Pattern of photodegradation of Quinoline Yellow.

4. Conclusions

This study investigates a microwave-assisted method for synthesizing nanomaterials, emphasizing its speed and environmental friendliness in a single-step process. Pure and iron-doped ZnS nanoparticles were synthesized directly in aqueous solution within 15 min at 140 °C using a microwave digestion reactor. The nanoparticles exhibited predominantly spherical shapes, sizes less than 5 nm, and face-centered cubic structures. Additionally, doped ZnS nanoparticles showed magnetic properties not observed in pure ZnS.

Both types of nanoparticles exhibited a characteristic ultraviolet absorption peak (~316 nm), indicating intrinsic absorption where electrons transitioned from the valence band to the conduction band. Interestingly, iron-doped ZnS nanoparticles only displayed a trap peak (~468 nm), suggesting energy level transitions of Fe ions that suppress the main UV emission peak observed in pure ZnS nanoparticles. Furthermore, doped nanoparticles demonstrated superior stability in water compared to pure ZnS, particularly evident at lower dopant concentrations (1% Fe).

Photodegradation studies revealed that even at a low concentration of iron ions (1% Fe), the photocatalytic efficiency of ZnS nanoparticles was significantly enhanced, achieving a 66.3% degradation of Quinoline Yellow within the initial 270 min when using 500 ppm. This enhancement is attributed to the doped nanoparticles' enhanced capability to generate reactive oxygen species or directly interact with Quinoline Yellow molecules through electron-hole pairs, thereby facilitating their degradation.

In conclusion, the use of microwave-assisted synthesis represents a promising technique for rapidly and efficiently generating iron-doped ZnS nanoparticles in a single step. These nanoparticles exhibit enhanced stability in water and possess significant photocatalytic properties for the degradation of contaminants. The method's ability to produce stable and effective nanocatalysts underscores its potential in advancing environmental remediation strategies, particularly in the field of water purification and wastewater treatment.

Scaling up the synthesis of iron-doped ZnS nanoparticles for photodegradation processes is challenging because large-scale production tends to vary in uniformity and quality due to variations in temperature and reactant concentrations. To address these issues, continuous-flow microwave reactors and automated synthesis systems can be employed. These technologies provide precise control over reaction conditions, enhancing reproducibility and efficiency, and ensuring consistent production of high-quality nanoparticles. Integrating real-time monitoring can further optimize the process, making large-scale production more feasible and cost-effective.

Author Contributions: Conceptualization, S.J.B.-R.; Funding acquisition, S.J.B.-R. and Y.C.-M.; Methodology, S.J.B.-R., A.M.N.-C. and K.T.-T.; Writing—original draft, S.J.B.-R. and Y.C.-M.; Writing—review and editing, Y.C.-M. All authors have read and agreed to the published version of the manuscript.

Funding: This research was funded by the National Science Foundation under Grant No. 2313252.

Data Availability Statement: The data related to this work are not publicly available but can be obtained from the corresponding author upon reasonable request.

Acknowledgments: TEM analyses were performed at the National High Magnetic Field Laboratory, supported by National Science Foundation Cooperative Agreement No. DMR-2128556 and the State of Florida. XRD and VSM measurements were performed at the Materials Characterization Laboratories from the Materials Science and Engineering Department of the University of Puerto Rico, Mayagüez Campus.

Conflicts of Interest: The authors declare no conflicts of interest.

References

1. Kumari, P.; Srivastava, A.; Sharma, R.K.; Sharma, D.; Srivastava, S.K. Zinc Oxide: A Fascinating Material for Photovoltaic Applications. In *Nanomaterials for Innovative Energy Systems and Devices*; Khan, Z.H., Ed.; Springer Nature: Singapore, 2022; pp. 173–241, ISBN 978-981-19055-3-7.
2. Ding, M.; Guo, Z.; Zhou, L.; Fang, X.; Zhang, L.; Zeng, L.; Xie, L.; Zhao, H. One-Dimensional Zinc Oxide Nanomaterials for Application in High-Performance Advanced Optoelectronic Devices. *Crystals* **2018**, *8*, 223. [CrossRef]
3. Yang, X.; Chung, E.; Johnston, I.; Ren, G.; Cheong, Y.-K. Exploitation of Antimicrobial Nanoparticles and Their Applications in Biomedical Engineering. *Appl. Sci.* **2021**, *11*, 4520. [CrossRef]
4. Klink, M.J.; Laloo, N.; Leudjo Taka, A.; Pakade, V.E.; Monapathi, M.E.; Modise, J.S. Synthesis, Characterization and Antimicrobial Activity of Zinc Oxide Nanoparticles against Selected Waterborne Bacterial and Yeast Pathogens. *Molecules* **2022**, *27*, 3532. [CrossRef] [PubMed]
5. Puspasari, V.; Ridhova, A.; Hermawan, A.; Amal, M.I.; Khan, M.M. ZnO-Based Antimicrobial Coatings for Biomedical Applications. *Bioprocess Biosyst. Eng.* **2022**, *45*, 1421–1445. [CrossRef] [PubMed]
6. Martínez-Carmona, M.; Gun'ko, Y.; Vallet-Regí, M. ZnO Nanostructures for Drug Delivery and Theranostic Applications. *Nanomaterials* **2018**, *8*, 268. [CrossRef]
7. Sathishkumar, P.; Li, Z.; Govindan, R.; Jayakumar, R.; Wang, C.; Long Gu, F. Zinc Oxide-Quercetin Nanocomposite as a Smart Nano-Drug Delivery System: Molecular-Level Interaction Studies. *Appl. Surf. Sci.* **2021**, *536*, 147741. [CrossRef]
8. Leone, F.; Cataldo, R.; Mohamed, S.S.Y.; Manna, L.; Banchero, M.; Ronchetti, S.; Mandras, N.; Tullio, V.; Cavalli, R.; Onida, B. Nanostructured ZnO as Multifunctional Carrier for a Green Antibacterial Drug Delivery System—A Feasibility Study. *Nanomaterials* **2019**, *9*, 407. [CrossRef]
9. Lahariya, V.; Ramrakhiani, M. Luminescence Study on Mn, Ni Co-Doped Zinc Sulfide Nanocrystals. *Luminescence* **2020**, *35*, 924–933. [CrossRef]
10. Tajoli, F.; Dengo, N.; Mognato, M.; Dolcet, P.; Lucchini, G.; Faresin, A.; Grunwaldt, J.-D.; Huang, X.; Badocco, D.; Maggini, M.; et al. Microfluidic Crystallization of Surfactant-Free Doped Zinc Sulfide Nanoparticles for Optical Bioimaging Applications. *ACS Appl. Mater. Interfaces* **2020**, *12*, 44074–44087. [CrossRef]

11. Mostafa, M.; El Nady, J.; Ebrahim, S.M.; Elshaer, A.M. Synthesis, Structural, and Optical Properties of Mn^{2+} Doped ZnS Quantum Dots for Biosensor Application. *Opt. Mater.* **2021**, *112*, 110732. [CrossRef]
12. Ghasemi, H.; Mozaffari, M.H.; Moradian, R. Effects of Deposition Time on Structural and Optical Properties of ZnS and ZnS/Au Thin Films Grown by Thermal Evaporation. *Phys. B Condens. Matter* **2022**, *627*, 413616. [CrossRef]
13. Xu, X.; Li, S.; Chen, J.; Cai, S.; Long, Z.; Fang, X. Design Principles and Material Engineering of ZnS for Optoelectronic Devices and Catalysis. *Adv. Funct. Mater.* **2018**, *28*, 1802029. [CrossRef]
14. Sun, C.; Gu, Y.; Wen, W.; Zhao, L. ZnSe Based Semiconductor Core-Shell Structures: From Preparation to Application. *Opt. Mater.* **2018**, *81*, 12–22. [CrossRef]
15. Zhang, Q.; Li, H.; Ma, Y.; Zhai, T. ZnSe Nanostructures: Synthesis, Properties and Applications. *Prog. Mater. Sci.* **2016**, *83*, 472–535. [CrossRef]
16. Zhang, J.; Wang, J.; Yan, T.; Peng, Y.; Xu, D.; Deng, D. InP/ZnSe/ZnS Quantum Dots with Strong Dual Emissions: Visible Excitonic Emission and near-Infrared Surface Defect Emission and Their Application In Vitro and In Vivo Bioimaging. *J. Mater. Chem. B* **2017**, *5*, 8152–8160. [CrossRef]
17. Aswathy, R.G.; Yoshida, Y.; Maekawa, T.; Kumar, D.S. Near-Infrared Quantum Dots for Deep Tissue Imaging. *Anal. Bioanal. Chem.* **2010**, *397*, 1417–1435. [CrossRef]
18. Talaiekhozani, A.; Rezania, S.; Kim, K.-H.; Sanaye, R.; Amani, A.M. Recent Advances in Photocatalytic Removal of Organic and Inorganic Pollutants in Air. *J. Clean. Prod.* **2021**, *278*, 123895. [CrossRef]
19. Bui, V.K.H.; Nguyen, T.N.; Van Tran, V.; Hur, J.; Kim, I.T.; Park, D.; Lee, Y.-C. Photocatalytic Materials for Indoor Air Purification Systems: An Updated Mini-Review. *Environ. Technol. Innov.* **2021**, *22*, 101471. [CrossRef]
20. Spoială, A.; Ilie, C.-I.; Trușcă, R.-D.; Oprea, O.-C.; Surdu, V.-A.; Vasile, B.Ș.; Ficai, A.; Ficai, D.; Andronescu, E.; Dițu, L.-M. Zinc Oxide Nanoparticles for Water Purification. *Materials* **2021**, *14*, 4747. [CrossRef]
21. Sultana, K.A.; Islam, M.T.; Silva, J.A.; Turley, R.S.; Hernandez-Viezcas, J.A.; Gardea-Torresdey, J.L.; Noveron, J.C. Sustainable Synthesis of Zinc Oxide Nanoparticles for Photocatalytic Degradation of Organic Pollutant and Generation of Hydroxyl Radical. *J. Mol. Liq.* **2020**, *307*, 112931. [CrossRef]
22. Ong, C.B.; Ng, L.Y.; Mohammad, A.W. A Review of ZnO Nanoparticles as Solar Photocatalysts: Synthesis, Mechanisms and Applications. *Renew. Sustain. Energy Rev.* **2018**, *81*, 536–551. [CrossRef]
23. Som, I.; Roy, M.; Saha, R. Advances in Nanomaterial-Based Water Treatment Approaches for Photocatalytic Degradation of Water Pollutants. *ChemCatChem* **2020**, *12*, 3409–3433. [CrossRef]
24. Raizada, P.; Sudhaik, A.; Singh, P. Photocatalytic Water Decontamination Using Graphene and ZnO Coupled Photocatalysts: A Review. *Mater. Sci. Energy Technol.* **2019**, *2*, 509–525. [CrossRef]
25. Tatarchuk, T.; Peter, A.; Al-Najar, B.; Vijaya, J.; Bououdina, M. Photocatalysis: Activity of Nanomaterials. In *Nanotechnology in Environmental Science*; John Wiley & Sons, Ltd.: Hoboken, NJ, USA, 2018; pp. 209–292, ISBN 978-3-527-80885-4.
26. Folawewo, A.D.; Bala, M.D. Nanocomposite Zinc Oxide-Based Photocatalysts: Recent Developments in Their Use for the Treatment of Dye-Polluted Wastewater. *Water* **2022**, *14*, 3899. [CrossRef]
27. Bailon-Ruiz, S.J.; Cedeño-Mattei, Y.; Torres-Torres, K.; Alamo-Nole, L. Photodegradation of Tropaeolin O in the Presence of Ag-Doped ZnO Nanoparticles. *Micro* **2023**, *3*, 643–652. [CrossRef]
28. Wagh, S.S.; Kadam, V.S.; Jagtap, C.V.; Salunkhe, D.B.; Patil, R.S.; Pathan, H.M.; Patole, S.P. Comparative Studies on Synthesis, Characterization and Photocatalytic Activity of Ag Doped ZnO Nanoparticles. *ACS Omega* **2023**, *8*, 7779–7790. [CrossRef]
29. Ghorai, S.; Patra, N.; Pal, A.; Bhattacharyya, D.; Jha, S.N.; Ray, B.; Chatterjee, S.; Ghosh, A.K. Insights into Local Atomic Structure of Fe Alloyed ZnS Nano Crystals: Correlation with Structural, Optical, Magnetic and Photocatalyst Properties. *J. Alloys Compd.* **2019**, *805*, 363–378. [CrossRef]
30. Zafar, S.; Zubair, M.; Shah, S.M.; Khan, M.I.; Khan, A.A.; Iqbal, M.F.; Hassan, A.; Din, M.F.U. Effect of Fe Doping on the Structural and Optical Properties of ZnS Macro-Spheres. *Optik* **2022**, *262*, 169342. [CrossRef]
31. Jrad, A.; Naouai, M.; Abdallah, A.; Ammar, S.; Turki-Kamoun, N. Doping ZnS Films with Cobalt: Structural, Compositional, Morphological, Optical, Electrical, Magnetic and Photocatalytic Properties. *Phys. B Condens. Matter* **2021**, *603*, 412776. [CrossRef]
32. Manivannan, N.; Chandar Shekar, B.; Senthil Kumaran, C.K.; Sugapriya, S. Structural, Morphological, Opto-Luminescence and Magnetic Behavioral Variations of Co–ZnS Hybrid Nanoparticles. *Indian J. Phys.* **2020**, *94*, 919–925. [CrossRef]
33. Sheraz Khan, M.; Shi, L.; Zou, B.; Ali, S. Theoretical Investigation of Optoelectronic and Magnetic Properties of Co-Doped ZnS and (Al, Co) Co-Doped ZnS. *Comput. Mater. Sci.* **2020**, *174*, 109491. [CrossRef]
34. Bhakta, N.; Chakrabarti, P.K. Defect Induced Room Temperature Ferromagnetism and Optical Properties of (Co, Y) Co-Doped ZnO Nanoparticles. *J. Magn. Magn. Mater.* **2019**, *485*, 419–426. [CrossRef]
35. Singh, N.K.; Koutu, V.; Malik, M.M. Enhancement of Room Temperature Ferromagnetic Behavior of Co-Doped ZnO Nanoparticles Synthesized via Sol–Gel Technique. *J. Sol-Gel Sci. Technol.* **2019**, *91*, 324–334. [CrossRef]
36. Ji, H.; Cai, C.; Zhou, S.; Liu, W. Structure, Photoluminescence, and Magnetic Properties of Co-Doped ZnO Nanoparticles. *J. Mater. Sci. Mater. Electron.* **2018**, *29*, 12917–12926. [CrossRef]
37. Basha, S.J.; Sarma, G.V.S.S.; Khidhirbrahmendra, V.; Rajyalakshmi, T.; Swetha, D.; Ravikumar, R.V.S.S.N. Enhanced Magnetic Properties of Fe^{3+} Doped ZnS Nanocrystals via Low Temperature Co-Precipitation: Spintronic and Nano-Device Applications. *Phys. Scr.* **2020**, *95*, 105802. [CrossRef]

38. Krsmanović Whiffen, R.; Montone, A.; Pietrelli, L.; Pilloni, L. On Tailoring Co-Precipitation Synthesis to Maximize Production Yield of Nanocrystalline Wurtzite ZnS. *Nanomaterials* **2021**, *11*, 715. [CrossRef]
39. Mandal, S.; Ali, S.I.; Mandal, A.C. Investigation of Structural, Optical and Photoluminescence Properties of the Sol–Gel Synthesized Powder ZnS Nanoparticles. *Appl. Phys. A* **2023**, *129*, 219. [CrossRef]
40. Gupta, P.; Patel, P.; Sujata, K.; Litoriya, P.K.; Solanki, R.G. Facile Synthesis and Characterization of ZnSe Nanoparticles. *Mater. Today Proc.* **2023**, *80*, 1556–1561. [CrossRef]
41. Wu, K.; Zhou, L.; Mao, C.; Chu, Y. Solvothermal Synthesis of ZnO with Controllable Morphology. *Mater. Lett.* **2023**, *341*, 134161. [CrossRef]
42. Kubiak, A.; Żółtowska, S.; Gabała, E.; Szybowicz, M.; Siwińska-Ciesielczyk, K.; Jesionowski, T. Controlled Microwave-Assisted and pH-Affected Growth of ZnO Structures and Their Photocatalytic Performance. *Powder Technol.* **2021**, *386*, 221–235. [CrossRef]
43. Salah, N.; AL-Shawafi, W.M.; Alshahrie, A.; Baghdadi, N.; Soliman, Y.M.; Memic, A. Size Controlled, Antimicrobial ZnO Nanostructures Produced by the Microwave Assisted Route. *Mater. Sci. Eng. C* **2019**, *99*, 1164–1173. [CrossRef]
44. Wang, W.; Lee, G.-J.; Wang, P.; Qiao, Z.; Liu, N.; Wu, J.J. Microwave Synthesis of Metal-Doped ZnS Photocatalysts and Applications on Degrading 4-Chlorophenol Using Heterogeneous Photocatalytic Ozonation Process. *Sep. Purif. Technol.* **2020**, *237*, 116469. [CrossRef]
45. Jubeer, E.M.; Manthrammel, M.A.; Shkir, M.; Subha, P.A.; Yahia, I.S.; Alfaify, S.A. Microwave Assisted Synthesis of Quantum Dots like ZnS Nanoparticles for Optoelectronic Applications: An Effect of CTAB Concentrations. *Optik* **2021**, *240*, 166812. [CrossRef]
46. Sanchez Tobon, C.; Ljubas, D.; Mandić, V.; Panžić, I.; Matijašić, G.; Ćurković, L. Microwave-Assisted Synthesis of N/TiO_2 Nanoparticles for Photocatalysis under Different Irradiation Spectra. *Nanomaterials* **2022**, *12*, 1473. [CrossRef]
47. Takeuchi, M.; Kishihara, M.; Fukuoka, T.; Yamaguchi, A.; Utsumi, Y. On Chip Synthesis of Au Nanoparticles by Microwave Heating. *Electron. Commun. Jpn.* **2020**, *103*, 49–55. [CrossRef]
48. Marinoiu, A.; Andrei, R.; Vagner, I.; Niculescu, V.; Bucura, F.; Constantinescu, M.; Carcadea, E. One Step Synthesis of Au Nanoparticles Supported on Graphene Oxide Using an Eco-Friendly Microwave-Assisted Process. *Mater. Sci.* **2020**, *26*, 249–254. [CrossRef]
49. Phuruangrat, A.; Siri, S.; Wadbua, P.; Thongtem, S.; Thongtem, T. Microwave-Assisted Synthesis, Photocatalysis and Antibacterial Activity of Ag Nanoparticles Supported on ZnO Flowers. *J. Phys. Chem. Solids* **2019**, *126*, 170–177. [CrossRef]
50. Kumar, R.; Youssry, S.M.; Abdel-Galeil, M.M.; Matsuda, A. One-Pot Synthesis of Reduced Graphene Oxide Nanosheets Anchored ZnO Nanoparticles via Microwave Approach for Electrochemical Performance as Supercapacitor Electrode. *J. Mater. Sci. Mater. Electron.* **2020**, *31*, 15456–15465. [CrossRef]
51. Xie, X.; Zhou, Y.; Huang, K. Advances in Microwave-Assisted Production of Reduced Graphene Oxide. *Front. Chem.* **2019**, *7*, 355. [CrossRef]
52. Sathya, A.; Kalyani, S.; Ranoo, S.; Philip, J. One-Step Microwave-Assisted Synthesis of Water-Dispersible Fe_3O_4 Magnetic Nanoclusters for Hyperthermia Applications. *J. Magn. Magn. Mater.* **2017**, *439*, 107–113. [CrossRef]
53. Banc, R.; Filip, L.; Cozma-Petrut, A.; Ciobarca, D.; Miere, D. Yellow and Red Synthetic Food Dyes and Potential Health Hazards: A Mini Review. *Bull. Univ. Agric. Sci. Vet. Med. Cluj-Napoca. Food Sci. Technol.* **2024**, *81*, 1–17.
54. Bailon-Ruiz, S.; Perales-Perez, O.J. Generation of singlet oxygen by water-stable CdSe(S) and ZnSe(S) quantum dots. *Appl. Mater. Today* **2017**, *9*, 161–166. [CrossRef]
55. Lugo-Ruiz, A.A.; Paz-Ruiz, M.J.; Bailón-Ruiz, S.J. Degradation of Organic Dyes in the Presence of Activated Titanium-Based Nanoparticles. *MRS Adv.* **2022**, *7*, 289–294. [CrossRef]
56. Nash-Montes, V.I.; Luciano-Velazquez, J.; Correa-Vargas, K.D.; Torres-Torres, K.N.; Bailón-Ruiz, S.J. Effect of the Capping Agent on the Photocatalytic Performance of ZnS Nanostructures. *MRS Adv.* **2022**, *7*, 203–207. [CrossRef]
57. Lopés-Velasco, N.M.; Bailón-Ruiz, S.J. Effect of the Particle Size and pH on the Photocatalytic Performance of Cerium Oxide (CeO_2) Nanoparticles. *MRS Adv.* **2021**, *6*, 769–773. [CrossRef]
58. Kustov, L.; Vikanova, K. Synthesis of Metal Nanoparticles under Microwave Irradiation: Get Much with Less Energy. *Metals* **2023**, *13*, 1714. [CrossRef]
59. Shahi, A.K.; Pandey, B.K.; Singh, B.P.; Gupta, B.K.; Singh, S.; Gopal, R. Photo Physical Studies of PVP Arrested ZnS Quantum Dots. *Electron. Mater. Lett.* **2017**, *13*, 160–167. [CrossRef]
60. Mishra, R.K.; Choi, G.-J.; Choi, H.-J.; Gwag, J.-S. ZnS Quantum Dot Based Acetone Sensor for Monitoring Health-Hazardous Gases in Indoor/Outdoor Environment. *Micromachines* **2021**, *12*, 598. [CrossRef] [PubMed]
61. Al-Badaii, F.; Al-Khalidy, A.; Khalid, M.; Al-Jarfi, A.; Al-Ansi, F.; Al-Jarfi, A.; Al-Nujaimi, N.; Al-Haj, A.; Halim, A.; Alnehia, A.; et al. Green Synthesis of Zinc Oxide Nanoparticles Using Allium Sativum Extract: Evaluation of Antibacterial Activity Against Nosocomial Bacteria. *Thamar Univ. J. Nat. Appl. Sci.* **2024**, *9*, 14–19. [CrossRef]
62. Mintcheva, N.; Gicheva, G.; Panayotova, M.; Wunderlich, W.; Kuchmizhak, A.A.; Kulinich, S.A. Preparation and Photocatalytic Properties of CdS and ZnS Nanomaterials Derived from Metal Xanthate. *Materials* **2019**, *12*, 3313. [CrossRef]
63. Murugadoss, G. Synthesis and Optical Characterization of PVP and SHMP-Encapsulated Mn^{2+}-Doped ZnS Nanocrystals. *J. Lumin.* **2010**, *130*, 2207–2214. [CrossRef]
64. Cao, X.; Shen, F.; Zhang, M.; Bie, J.; Liu, X.; Luo, Y.; Guo, J.; Sun, C. Facile Synthesis of Chitosan-Capped ZnS Quantum Dots as an Eco-Friendly Fluorescence Sensor for Rapid Determination of Bisphenol A in Water and Plastic Samples. *RSC Adv.* **2014**, *4*, 16597–16606. [CrossRef]

65. Bhushan, M.; Jha, R.; Bhardwaj, R. Reduced Band Gap and Diffusion Controlled Spherical N-Type ZnS Nanoparticles for Absorption of UV-Vis Region of Solar Spectrum. *J. Phys. Chem. Solids* **2019**, *135*, 109021. [CrossRef]
66. Ciciliati, M.A.; Silva, M.F.; Fernandes, D.M.; de Melo, M.A.C.; Hechenleitner, A.A.W.; Pineda, E.A.G. Fe-Doped ZnO Nanoparticles: Synthesis by a Modified Sol–Gel Method and Characterization. *Mater. Lett.* **2015**, *159*, 84–86. [CrossRef]
67. Gudla, U.R.; Suryanarayana, B.; Raghavendra, V.; Emmanuel, K.A.; Murali, N.; Taddesse, P.; Parajuli, D.; Chandra Babu Naidu, K.; Ramakrishna, Y.; Chandramouli, K. Optical and Luminescence Properties of Pure, Iron-Doped, and Glucose Capped ZnO Nanoparticles. *Results Phys.* **2020**, *19*, 103508. [CrossRef]
68. Ovhal, M.M.; Santhosh Kumar, A.; Khullar, P.; Kumar, M.; Abhyankar, A.C. Photoluminescence Quenching and Enhanced Spin Relaxation in Fe Doped ZnO Nanoparticles. *Mater. Chem. Phys.* **2017**, *195*, 58–66. [CrossRef]
69. Carofiglio, M.; Conte, M.; Racca, L.; Cauda, V. Synergistic Phenomena between Iron-Doped ZnO Nanoparticles and Shock Waves Exploited against Pancreatic Cancer Cells. *ACS Appl. Nano Mater.* **2022**, *5*, 17212–17225. [CrossRef]
70. Tab, A.; Dahmane, M.; Chemseddin, B.; Bellal, B.; Trari, M.; Richard, C. Photocatalytic Degradation of Quinoline Yellow over Ag_3PO_4. *Catalysts* **2020**, *10*, 1461. [CrossRef]
71. Kareem, M.; Bello, I.; Shittu, H.; Prakash, P.S.; Adedokun, O.; Arumugam, S. Synthesis, Characterization, and Photocatalytic Application of Silver Doped Zinc Oxide Nanoparticles. *Clean. Mater.* **2022**, *3*, 100041. [CrossRef]
72. Joe, A.; Park, S.-H.; Kim, D.-J.; Lee, Y.-J.; Jhee, K.-H.; Sohn, Y.; Jang, E.-S. Antimicrobial Activity of ZnO Nanoplates and Its Ag Nanocomposites: Insight into an ROS-Mediated Antibacterial Mechanism under UV Light. *J. Solid State Chem.* **2018**, *267*, 124–133. [CrossRef]